


Article

Estimation of the Block Adjustment Error in UAV Photogrammetric Flights in Flat Areas

Alba Nely Arévalo-Verjel ^{1,2}, José Luis Lerma ^{1,*} , Juan F. Prieto ³ , Juan Pedro Carbonell-Rivera ⁴ 
and José Fernández ⁵ 

¹ Grupo de Investigación en Fotogrametría y Láser Escáner (GIFLE), Departamento de Ingeniería Cartográfica, Geodesia y Fotogrametría, Universitat Politècnica de València, Camino de Vera s/n, 46022 Valencia, Spain; alarver@doctor.upv.es

² Grupo de Investigación en Hidrología y Recursos Hídricos (HYDROS), Departamento de Construcciones Civiles, Universidad Francisco de Paula Santander, Cúcuta 540003, Colombia

³ ETSI Topografía, Geodesia y Cartografía, Universidad Politécnica de Madrid, Ctra. Valencia km 7, 28031 Madrid, Spain; juanf.prieto@upm.es

⁴ Geo-Environmental Cartography and Remote Sensing Group (CGAT), Universidad Politécnica de València, Camino de Vera s/n, 46022 Valencia, Spain; juacarri@upv.es

⁵ Institute of Geosciences (IGEO), CSIC-UCM, Calle del Doctor Severo Ochoa, 7, Ciudad Universitaria, 28040 Madrid, Spain; jft@mat.ucm.es

* Correspondence: jllerma@cgf.upv.es

Abstract: UAV-DAP (unmanned aerial vehicle-digital aerial photogrammetry) has become one of the most widely used geomatics techniques in the last decade due to its low cost and capacity to generate high-density point clouds, thus demonstrating its great potential for delivering high-precision products with a spatial resolution of centimetres. The question is, how should it be applied to obtain the best results? This research explores different flat scenarios to analyse the accuracy of this type of survey based on photogrammetric SfM (structure from motion) technology, flight planning with ground control points (GCPs), and the combination of forward and cross strips, up to the point of processing. The RMSE (root mean square error) is analysed for each scenario to verify the quality of the results. An equation is adjusted to estimate the a priori accuracy of the photogrammetric survey with digital sensors, identifying the best option for μ_{xyz} (weight coefficients depending on the layout of both the GCP and the image network) for the four scenarios studied. The UAV flights were made in Lorca (Murcia, Spain). The study area has an extension of 80 ha, which was divided into four blocks. The GCPs and checkpoints (ChPs) were measured using dual-frequency GNSS (global navigation satellite system), with a tripod and centring system on the mark at the indicated point. The photographs were post-processed using the Agisoft Metashape Professional software (64 bits). The flights were made with two multicopter UAVs, a Phantom 3 Professional and an Inspire 2, with a Zenmuse X5S camera. We verify the influence by including additional forward and/or cross strips combined with four GCPs in the corners, plus one additional GCP in the centre, in order to obtain better photogrammetric adjustments based on the preliminary flight planning.

Keywords: UAV; UAV-DAP; aerial close-range photogrammetry; GCP; flight planning



Citation: Arévalo-Verjel, A.N.; Lerma, J.L.; Prieto, J.F.; Carbonell-Rivera, J.P.; Fernández, J. Estimation of the Block Adjustment Error in UAV Photogrammetric Flights in Flat Areas. *Remote Sens.* **2022**, *14*, 2877. <https://doi.org/10.3390/rs14122877>

Academic Editors: Kamil Krasuski and Damian Wierzbicki

Received: 26 March 2022

Accepted: 11 June 2022

Published: 16 June 2022

Publisher's Note: MDPI stays neutral with regard to jurisdictional claims in published maps and institutional affiliations.



Copyright: © 2022 by the authors. Licensee MDPI, Basel, Switzerland. This article is an open access article distributed under the terms and conditions of the Creative Commons Attribution (CC BY) license (<https://creativecommons.org/licenses/by/4.0/>).

1. Introduction

UAVs have become a valuable platform for obtaining digital images, and are deployed as a measuring instrument for numerous geomatic and geospatial applications [1]. UAV-DAP, classified as close-range aerial photogrammetry, is a versatile, accessible, and economical topographical method that can be rapidly developed to reconstruct the surface geometry of 3D objects [2]. Although the equipment was initially used only for military purposes, this method is now more widely used in the world of geomatics [3]. This technique offers excellent potential for mapping and remote sensing (RS) and satisfies the market's needs for remote observation data.

UAV-DAP is one of the most widely used RS techniques in small extension studies, due to its flexibility in data acquisition, low operating costs, and high spatial and temporal resolution [3,4]. UAV-DAP is based on structure from motion (SfM) algorithms, and uses the high spatial resolution of photographs to recognise textures [5] and orient the photographs by identifying common points, without the need to know the camera parameters or the grid geometry [6]. It produces results such as digital surface models (DSM), contour lines and orthomosaics, which are used in a range of studies, such as the inspection and surveillance of natural risks [7], infrastructures or civil engineering works [8], calculating earth movements in open mines or quarries, levelling beaches [9], coastal monitoring [10], landslides monitoring [11], subsidence analysis [12], fire surveillance [13], precision agriculture [14], forest inventories [15], and vegetation monitoring [16].

Among the main advantages of UAV-DAP is its lower application cost compared to lidar (light detection and ranging) technology [17], while its results are similar in terms of precision and spatial resolution [18]. Compared to classic topography (GNSS, total station, tachymetry), one of the most important benefits is the generation of a dense cloud with less fieldwork. The UAV-DAP technique has a higher spatial resolution [19] than the satellite segment and allows data to be obtained under cloud cover.

There are currently a range of applications for planning and automating flights with UAV and photo processing programmes.

During the flight planning phase, it is necessary to know the legal aspects governing the flight, and to verify whether the study zone is within an urban or rural area and whether it is affected by any restrictions from the civil aviation authority. The regulations in each country (Ref. [20], for the case of Spain) and the general specifications of the equipment, contained in the manufacturer's manual, must be followed to operate the UAV. There is usually an obligation to obtain an operating licence in order to avoid accidents and prevent causing harm to third parties.

In regard to technical aspects, the correct location of the ground control points (GCPs), flight time, maximum sensor speed, and the orientation and position of the photographs to be captured must be established, and the programmed flight must be uploaded to the application to be used. It is important to consider the solar height and the GNSS satellite constellation, and to review any meteorological phenomena that directly impact the flight (Regulation (EU) 2019/947). There are also some general recommendations, such as determining the topography of the area using a digital elevation model (DEM), in the case of steep terrain, as this produces a better image cover and a more homogeneous ground sampling distance (GSD) [21]. On this type of terrain, or when there are occlusions, it is recommended to take oblique photographs to improve the orientation process and obtain more orthogonal shots of the subject.

The aspects that affect the accuracy of the camera orientation, and hence the photogrammetric outputs, include the loss of the GNSS signal and the transformations in the system of coordinates (image-terrain).

The GCPs allow the absolute orientation, transforming the solution to its position on the ground. In absolute orientation, the cartographic product is oriented, levelled, and scaled. In photogrammetric flights, the GCPs must therefore be taken strategically, preferably on the periphery or on the corners of the block for the planimetric component, so that the transmission error is minimal inside the block, in the case of regular surveys. Chains of GCPs located across the block should be used for altimetric control to reduce altimetric error; another option is to make cross strips at the ends of the block or every certain number of models, to minimise altimetric error, or in the case of surveys with several flights. Therefore, the strips are stabilised in the direction of the flight, producing a more stable solution [22].

The number of GCPs directly influences the model's accuracy [23–28]. In this sense, to increase the accuracy of the bundle block adjustment, it is recommended to understand the behaviour of the planimetric and altimetric errors based on the number of GCPs. For altimetry, the GCPs should be distributed across the flight lines along chains or cross strips

on the edges of the block [2,23]. However, currently, there is usually no distinction between planimetric control and altimetric control, and surveyors measure full XYZ coordinates. Besides, the absence of GCPs makes it challenging to detect coarse global errors [23,29].

The influence of the number of GCPs has been recently studied for UAVs based on the area studied. Table 1 summarises the error reported in different contributions, showing how a greater density of GCPs per hectare (ha) may not directly increase the accuracy of the photogrammetric bundle block adjustment.

Table 1. Studies on the number of GCP and their relation with the study area.

| Reference | GCP | AREA (ha) | Ratio GCP/ha | RMSE (cm) |
|-----------|-----|-----------|--------------|-----------|
| [2] | 3 | 0.02 | 150 | 52 |
| [29] | 45 | 1 | 45 | 0.23 |
| [27] | 5 | 0.83 | 6 | 6.2 |
| [25] | 27 | 5.0 | 5.4 | 6.6 |
| [23] | 7 | 1.5 | 4.6 | 51 |
| [30] | 5 | 2.73 | 1.83 | 3 |
| [31] | 15 | 12 | 1.25 | 14.3 |
| [32] | 20 | 17.6 | 1.13 | 3.6 |
| [24] | 15 | 17.6 | 0.85 | 5.8 |
| [26] | 11 | 37.4 | 0.29 | 5.9 |
| [33] | 6 | 38 | 0.15 | 1.3 |
| [28] | 102 | 1200 | 0.1 | 1 |
| [34] | 9 | 270 | 0.03 | 3.2 |

The main aim of this study is to demonstrate how the flight plan influences the results obtained with UAV-DAP by applying aerial triangulation with bundle block adjustment.

2. Materials and Methods

The study was conducted in Lorca (Murcia, Spain). The study zone has been continually monitored for ten years. It presents important subduction of the terrain due to the intensive overexploitation of the local aquifers, which has led to deformations in the vertical and horizontal components of up to 10 cm/year [35–38]. Prior to the flights, NOTAM information for the area to be flown was reviewed. The information was consulted on the geoportal dedicated to drone flights of the Spanish Aviation Safety and Security Agency (<https://drones.enaire.es/> accessed on 15 May 2021). A UAV photogrammetric survey was carried out during the field campaign (May 2021), dividing the area of interest into four blocks to cover a total area of 80 ha (Figure 1); the areas of each block are shown in Table 2, with the type of UAV used.

Table 2. Area in hectares for each block studied; h_f refers to the forward flight height, and h_c refers to cross flight height.

| Block | Strips Type | Area (ha) | UAV | Flight Height |
|---------------|----------------|-----------|---------------|---------------|
| Block 1 | Forward strips | 19.11 | Phantom 3 Pro | $h_f = 120$ m |
| Block 1 | Cross strip 1 | 0.8 | Inspire 2 | $h_c = 110$ m |
| Block 1 and 2 | Cross strip 2 | 0.8 | Inspire 2 | $h_c = 110$ m |
| Block 2 | Forward strips | 19.11 | Phantom 3 Pro | $h_f = 120$ m |
| Block 2 and 3 | Cross strip 3 | 0.8 | Inspire 2 | $h_c = 110$ m |
| Block 3 | Forward strips | 22.95 | Inspire 2 | $h_f = 120$ m |
| Block 3 and 4 | Cross strip 4 | 0.8 | Inspire 2 | $h_c = 110$ m |
| Block 4 | Forward strips | 18.86 | Phantom 3 Pro | $h_f = 120$ m |
| Block 4 | Cross strip 5 | 0.8 | Inspire 2 | $h_c = 110$ m |
| Total | | 84.03 | | |

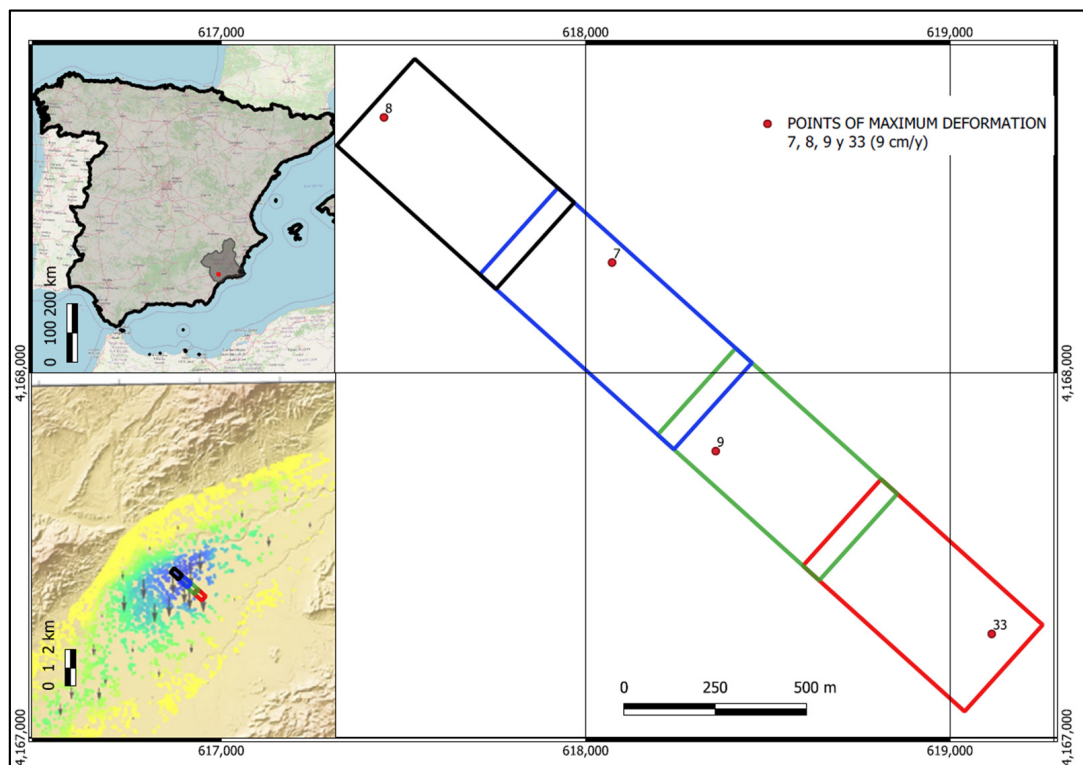


Figure 1. Location of the study area in Lorca, Vía Camino de Puente Alto; the coordinates for the reference system are UTM 30N ETRS89. Points 7,8,9,10,33 have the maximum deformation in the study of [35].

During the flights, there was a NOTAM in force in the area affecting Flight Level 100/Flight Level 220, issued by the General Air Academy based in San Javier (Murcia), so we had to coordinate operations with the control tower.

Two multirotor UAVs were used to acquire photogrammetric data: a DJI Phantom 3 Pro (Figure 2a) and a DJI Inspire 2, equipped with a Zenmuse X5S camera (Figure 2b). The camera specifications are shown in Table 3. The flights were made under a VLOS (Visual Line of Sight) operational scenario with the visual scope of the UAV, using the Dronedeploy application for the flight plan [39]. The meteorological conditions for the flights were optimal: a sunny day with calm winds.

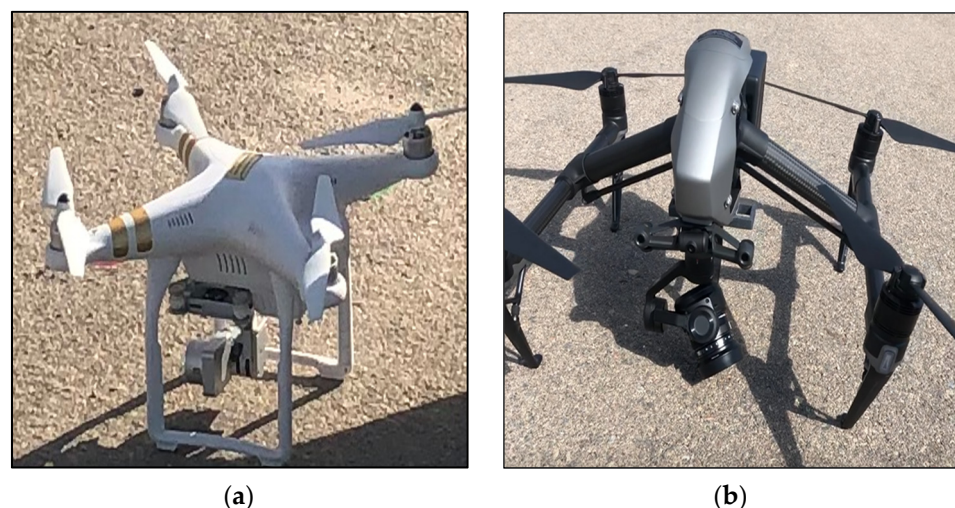


Figure 2. UAVs used in the study: (a) Phantom 3 Pro; (b) Inspire 2 with a Zenmuse X5S camera.

Table 3. Camera and image specifications for the Phantom 3 Pro and Inspire 2 UAV used in the study.

| Drone | Phantom 3 Pro | Inspire 2 |
|-------------------------------|--------------------|--------------------|
| Resolution | 4000 × 3000 pixels | 5280 × 3956 pixels |
| DJI | FC300X | Zenmuse X5S |
| F-stop | f/2.8 | f/1.7 |
| Focal distance | 4 mm | 15 mm |
| Equivalent 35 mm focal length | 20 | 30 |

2.1. GNSS Campaign

The GCPs and ChPs (check points), also known as ground evaluation points (GEP), were marked before the flight. This was done by creating a cardboard template of a target of 60 cm × 60 cm comprising three blades, each separated by 120°, and a central circle. Each point was marked using reflective white paint, and a survey nail was placed in the centre (Figure 3a).

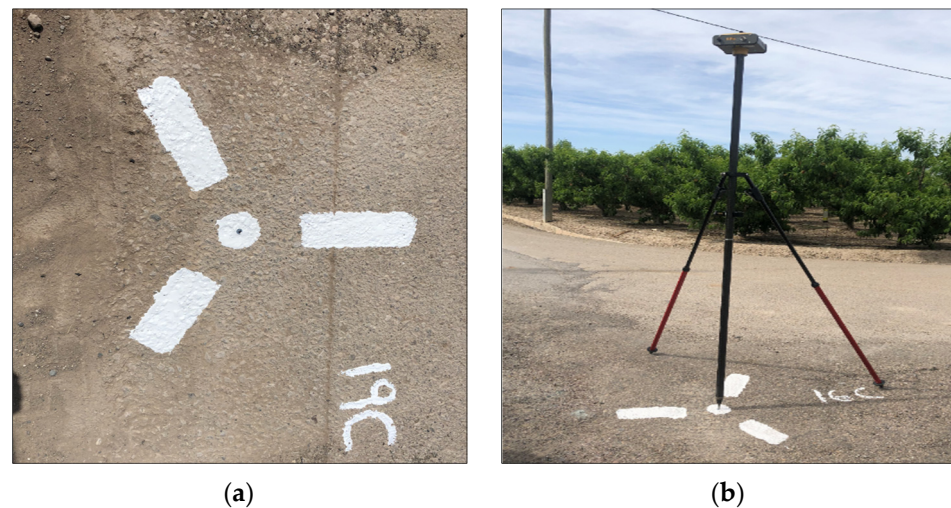


Figure 3. GCP: (a) target with three blades and a central circle with a nail in the centre; (b) dual-frequency GNSS receiver positioned on a tripod and centred on the point mark.

All the points (GCPs and ChPs) were measured with dual-frequency GNSS receivers (GPS + GLONASS) on a tripod and centred on the point mark (Figure 3b) for at least 15 min. All the points were measured twice with a different constellation and different receivers, which were configured for a static survey. A total of ten GCPs were measured, distributed at the four corners of each block, and nine ChPs were arranged randomly so that there were at least two ChPs in each block. The distribution of the points is shown in Figure 4. When designing this distribution, priority was given to ensuring that the points were located on the firm ground, such as roadways, and that no nearby elements would impede the satellite signal. The GCPs were positioned in the common areas between the blocks. Short cross flights were made in these same areas to optimise the UAV batteries and reduce the number of GCPs.

The precise geodetic ionospheric correction models of the CODE (Centre for Orbit Determination in Europe [40]) and the precise ephemerides of the IGS (International GNSS Service) [41] were used to calculate the GCPs and ChPs coordinates for both constellations. Data from 22 continuous stations were processed to improve the general network configuration and link the local measurements to a regional geodetic reference framework. These stations are located in the southeast of the Iberian Peninsula and are part of the regional networks of the Region of Murcia (REGAM and MERISTEMUM) and the Spanish National ERGNSS-IGN Network (National Geographic Institute), with 24 h and 30 s of observation over ten days. The GNSS vectors in the network were processed using Leica Infinity software, with absolute antenna calibration models and Vienna Mapping Functions

(VMF) [42] for the tropospheric modelling. Subsequently, the vectors previously obtained in the network were combined with their complete variance-covariance matrices using Microsearch GeoLab software. This allows the estimation of the whole set of coordinates of the network points on the ETRS89 system, with an independent weighting strategy based on the quality of the vectors following the methodology used in high-precision networks [43,44].

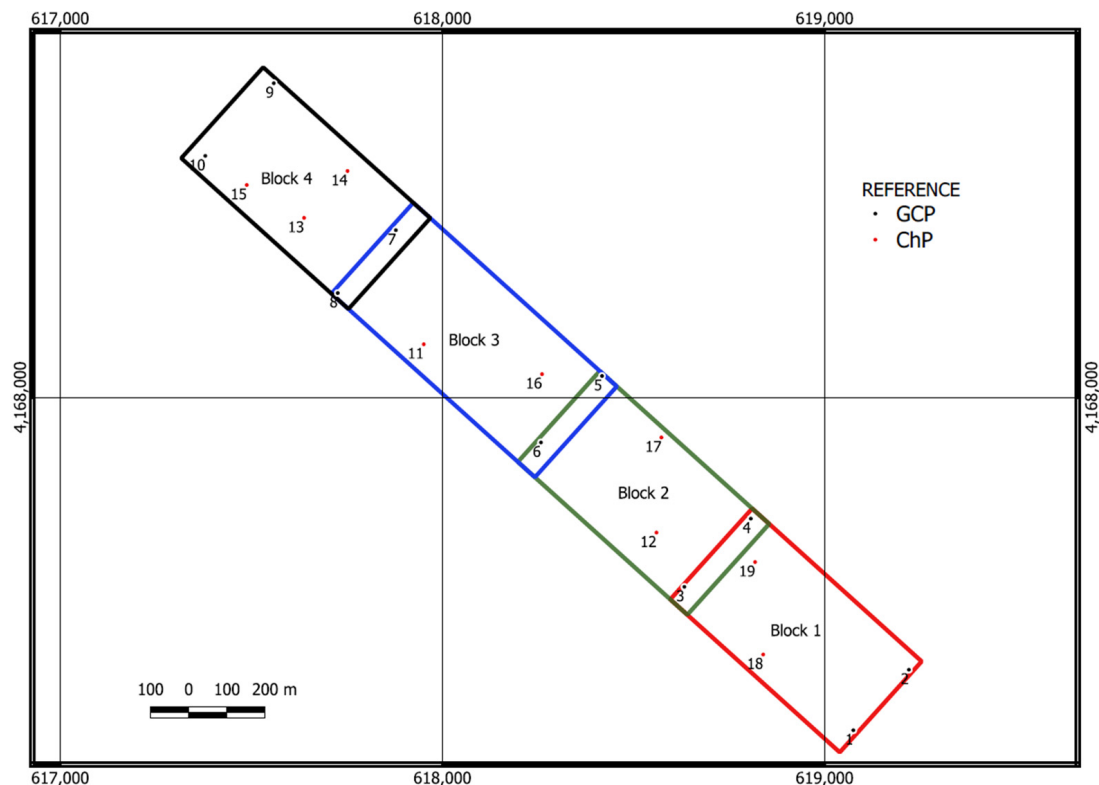


Figure 4. Location of the ten GCPs at the corners of each block and nine ChPs distributed within the blocks; the reference system is UTM 30N ETRS89.

2.2. Image Acquisition

Flights were planned with the DroneDeploy application for PC, which allows the importation of KML (Keyhole Markup Language) or KMZ (Keyhole Markup Language compressed). These formats are based on XML to store geographic data and related content, and are an official standard of the Open Geospatial Consortium (OGC) [45]. The flights were programmed prior to the data campaign, taking into account the autonomy of the equipment batteries and the study area; the blocks were imported to the DroneDeploy application in the KMZ format.

Three flight missions were carried out with the Phantom 3 Pro following the scheme in Figure 5a, and one with the Inspire 2 (Figure 5b) to cover the four blocks. Another five flight missions were completed with the Inspire 2 (Figure 5c) for the cross strip at the height of 110 m (h_c , cross flight height). The images were acquired orthogonally and with a forward and side overlap of over 60% [46]. The flight configurations were the following:

- Phantom 3 Pro: For Blocks 1,2, and 4, flight height (h_f) 120 m (the maximum allowed by Spanish regulation), forward overlap 80%, side overlap 60%, and speed 9 m/s for an area of 19 ha, with a GSD of 5.1 cm. The flight duration was 14'8'', taking 326 images for Block 1, 296 for Block 2, and 310 for Block 4.
- Inspire 2: Flight height 120 m (h_f), forward overlap 80%, side overlap 60%, speed 10 m/s for an area of 23 ha, with a GSD of 2.1 cm. The flight duration was 14'38'', taking a total of 327 images in Block 3.

- Inspire 2: Strip flight height 110 m (h_f), forward overlap 80%, side overlap 60%, speed 10 m/s for an area of 0.8 ha, with a GSD of 2.4 cm. The flight duration was 4'39'', taking a total of 74 images for each block.

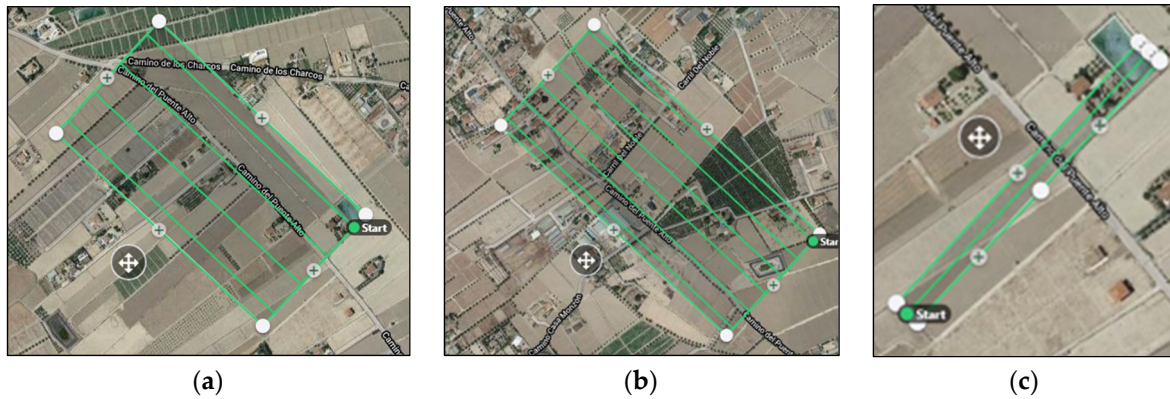


Figure 5. The flight programming was initially carried out with the DroneDeploy application: (a) Phantom 3 Pro, Block 1; (b) Inspire 2, Block 3; (c) cross strip Inspire2, Block 1.

For measuring 80 ha of the overall study area, it was divided into four areas (Figure 4) with its corresponding blocks (Figure 6), in a way such that a single set of UAV batteries was used for each block. Figure 6 displays the setup for the overall study area, Scenario C (next section).

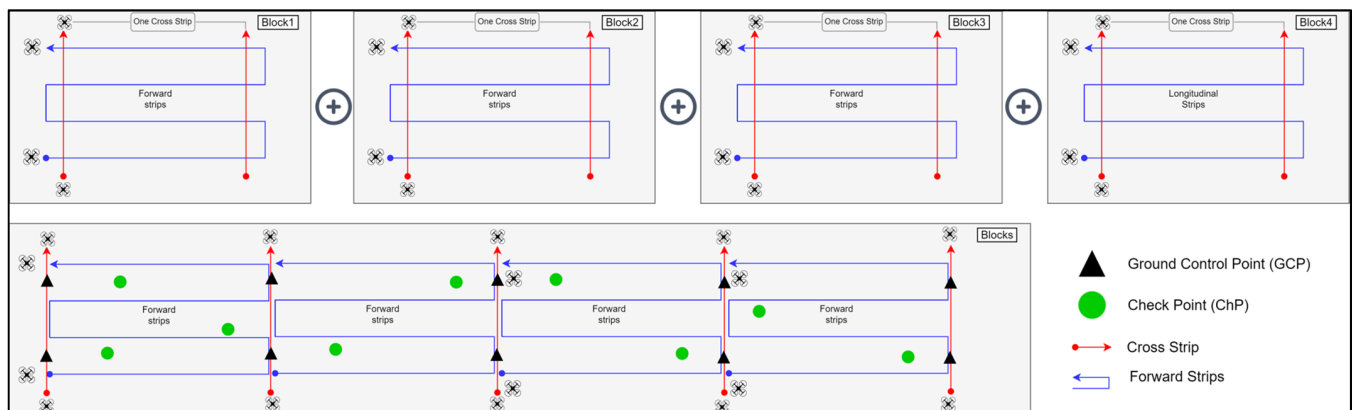


Figure 6. (Upper row) Study area distributed in four blocks. (Bottom row) Distribution of the flight lines for Scenario C.

2.3. Photogrammetric Processing

The data was processed using a laptop equipped with an ASUS processor Intel (R) Core (TM) i7 -4210U CPU 1.70 GHz 2.40 GHz, RAM 16 GB and an NVIDIA GEFORCE 820 M graphics card, running under Windows 10 (64 bits). The program used for processing the images was Agisoft Metashape Professional (64 bits), analysing several scenarios to generate the dense point cloud to compare and verify which of the four scenarios obtained the best results:

- Scenario A: Flight mission with flight strips, (example Block 1, Figure 7A).
- Scenario B: Flight mission with flight strips, in addition to a flight strip covering the whole perimeter of each block (example Block 1, Figure 7B).
- Scenario C: Flight mission with flight strips; in addition, one cross strip at both ends of each block (example Block 1, Figure 7C).
- Scenario D: Flight mission with flight strips; an additional strip covering the whole perimeter and two cross strips at both ends of each block (example Block 1, Figure 7D).

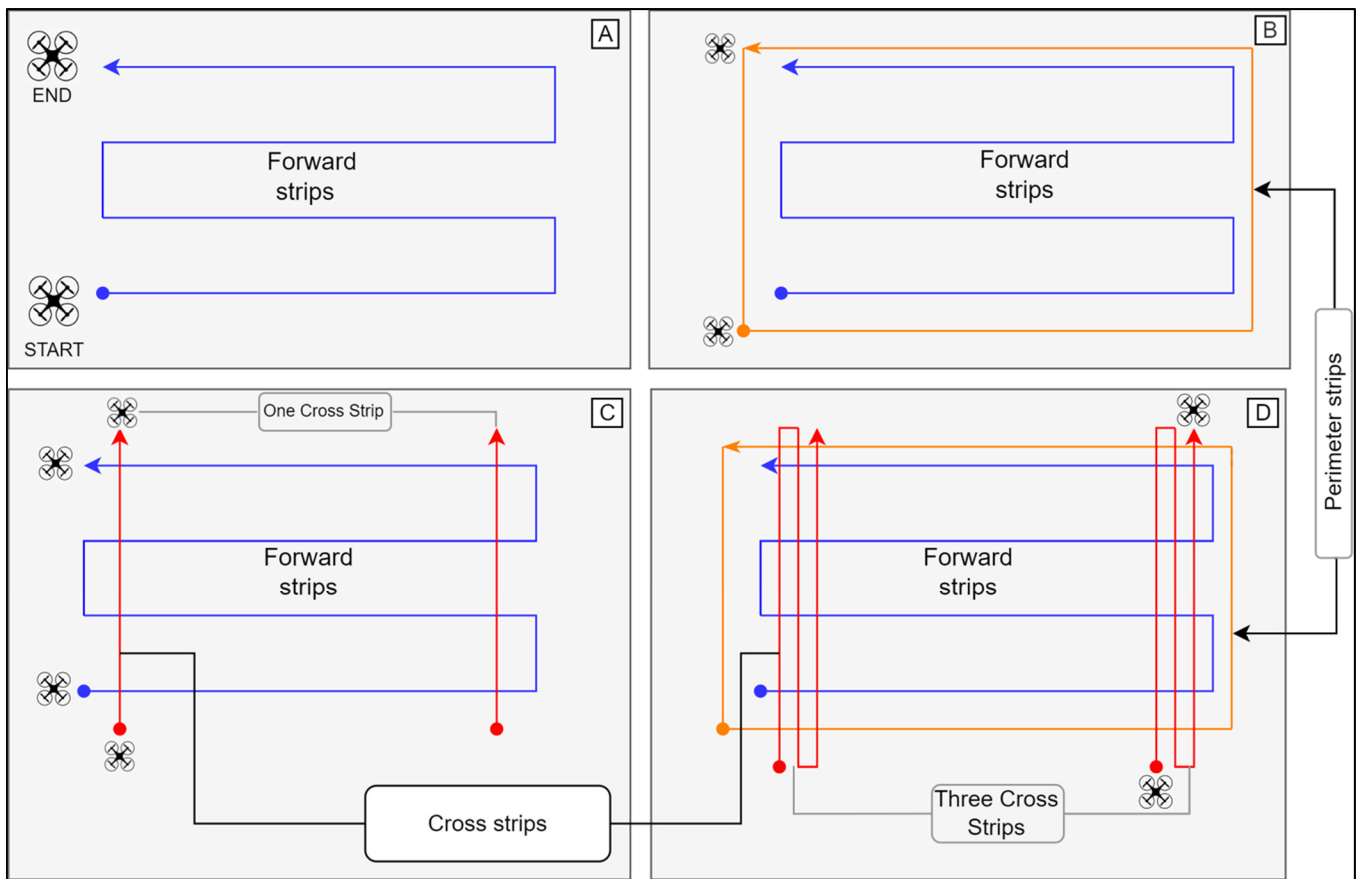


Figure 7. Processing of each scenario: (A) Scenario A, processing of photographs with conventional flight planning; (B) Scenario B, Scenario A plus the block perimeter; (C) Scenario C, Scenario A plus one cross strip at each edge; (D) Scenario D, Scenario B plus three cross strips at each edge.

Scenarios A, B, and C are image subsets of Scenario D.

2.4. Accuracy of the Results

For the evaluation of the results, two statistics were used: the a priori accuracy of the block and RMSE.

2.4.1. A Priori Accuracy of the Block

The estimation of the a priori planimetric error of the blocks with four GPSs at the edges (Scenario A) uses the next equation:

$$\sigma_{B,L} = (0.47 + 0.25n_s)\sigma_{M,L} \quad (1)$$

where:

$\sigma_{B,L}$ = estimated planimetric accuracy of the block ($L = XY$);

σ_o = sigma naught of the bundle block adjustment;

n_s = number of strips;

$\sigma_{M,L}$ = estimated planimetric accuracy of a single model.

Equation (1) was conceived for aerial photographs measured with analytical stereo-plotters [47]. For digital photogrammetry with digital sensors, we can rewrite Equation (1) as the following:

$$\sigma_{B,XYZ} = \mu_{xyz} * \sigma_o * GSD \quad (2)$$

where:

σ_o = sigma naught of the bundle block adjustment can be taken as the mean reprojection error of the adjustment.

μ_{xyz} = weight coefficients depending on the layout of both the GCP and the image network.

This paper seeks to identify the weight coefficients (μ_{xyz}) in Equation (2) for the four scenarios acquired by UAV, A, B, C, and D, in order to determine the best equation for the a priori accuracy estimation valid for the UAV-DAP with absolute GNSS on flat areas. To the authors' knowledge, no similar equation exists in the literature.

2.4.2. RMSE

The RMSE is calculated to determine the accuracy of the photogrammetric results. The square of the RMSE is equal to the arithmetic mean of the squares of the true errors [48], defined by the next equation:

$$\text{RMSE} = \sqrt{\frac{\sum_{i=1}^n (\text{XYZ} - \text{Control})^2}{n}} \quad (3)$$

where:

XYZ = photogrammetric coordinates;

Control = reference data (GCP and ChP) taken in the field with GNSS;

n = number of verification points.

3. Results

3.1. Results of the Global Navigation Satellite System (GNSS)

Table 4 shows the coordinates and uncertainties of the GCP and ChP, in addition to the four continuous stations located in the area near the study zone. The grid was finally adjusted with a loose restriction, taking into account the regional velocity field developed in [35,44]. The values of the uncertainties were calculated with a 95% confidence level.

Table 4. Coordinates of the GCP and the four continuous stations (ALHA, LORC, LRCA, and MAZA) for the observation period used for the adjustment; Microsearch GeoLab software, reference system UTM 30N ETRS89.

| Point | Coordinates (m) | | | Std (m) | | |
|--------|-----------------|---------------|----------|---------|-------|----------|
| | East | North | Altitude | East | North | Altitude |
| 1 GCP | 619,066.137 | 4,167,121.713 | 290.788 | 0.007 | 0.005 | 0.012 |
| 2 GCP | 619,228.593 | 4,167,279.381 | 291.107 | 0.006 | 0.004 | 0.010 |
| 3 GCP | 618,657.880 | 4,167,476.026 | 293.247 | 0.006 | 0.005 | 0.011 |
| 4 GCP | 618,807.284 | 4,167,654.158 | 293.218 | 0.006 | 0.005 | 0.010 |
| 5 GCP | 618,439.352 | 4,168,023.346 | 295.627 | 0.006 | 0.005 | 0.012 |
| 6 GCP | 618,252.834 | 4,167,885.737 | 296.434 | 0.005 | 0.004 | 0.011 |
| 7 GCP | 617,869.899 | 4,168,444.438 | 301.216 | 0.008 | 0.007 | 0.012 |
| 8 GCP | 617,725.688 | 4,168,267.210 | 301.212 | 0.005 | 0.004 | 0.008 |
| 9 GCP | 617,556.991 | 4,168,820.869 | 306.724 | 0.008 | 0.007 | 0.012 |
| 10 GCP | 617,373.720 | 4,168,634.016 | 305.914 | 0.007 | 0.006 | 0.011 |
| 11 ChP | 617,949.400 | 4,168,139.298 | 299.812 | 0.013 | 0.010 | 0.025 |
| 12 ChP | 618,565.778 | 4,167,644.981 | 294.215 | 0.009 | 0.007 | 0.017 |
| 13 ChP | 617,639.593 | 4,168,465.141 | 303.490 | 0.012 | 0.010 | 0.020 |
| 14 ChP | 617,775.094 | 4,168,586.984 | 301.914 | 0.010 | 0.008 | 0.018 |
| 15 ChP | 617,496.083 | 4,168,564.809 | 305.395 | 0.011 | 0.011 | 0.018 |
| 16 ChP | 618,259.189 | 4,168,060.380 | 296.895 | 0.005 | 0.004 | 0.009 |
| 17 ChP | 618,525.229 | 4,167,874.276 | 294.169 | 0.006 | 0.005 | 0.012 |
| 18 ChP | 618,839.705 | 4,167,325.172 | 292.311 | 0.009 | 0.007 | 0.016 |
| 19 ChP | 618,805.372 | 4,167,568.696 | 293.171 | 0.006 | 0.005 | 0.012 |
| ALHA | 636,738.931 | 4,185,231.011 | 201.790 | 0.003 | 0.003 | 0.004 |
| LORC | 615,840.139 | 4,168,225.450 | 313.952 | 0.003 | 0.002 | 0.003 |
| LRCA | 614,704.897 | 4,168,655.120 | 332.211 | 0.003 | 0.002 | 0.004 |
| MAZA | 649,154.772 | 4,162,049.757 | 55.060 | 0.002 | 0.002 | 0.003 |

3.2. Photogrammetric Flight Results

The results of the photogrammetric flight were divided into four blocks.

3.2.1. Block 1 Results

In Scenario A, 168 photographs were processed, containing the forward strips in the block (Figure 7A); 268 photographs were processed in Scenario B (Figure 7B); 200 photographs were processed in Scenario C (Figure 7C); and 334 photographs were processed in Scenario D (Figure 7D). The workflow was processed in Agisoft Metashape [46]. The high-precision configuration was used to orient the images, meaning that the position and orientation of the camera were calculated for each image, and the tie points were extracted in the form of disperse point clouds [28]. The GCPs and ChPs were then marked, as shown in [33]. The points were measured with a minimum of 13 and a maximum of 22 photos, which is a favourable amount, as the larger the number of photos marked, the greater the redundancy. The accuracy of the projection centres was set at 10 m, camera rotations at 10 deg, the accuracy of the GCPs was set at 0.007 mm, the markers at 0.5 pix, and the tie points at 1 pix. The results of the RMSE of the GCPs for Block 1 are shown in Table 5, leaving points 1, 2, 3, and 4 at the corners of the block as GCPs, and points 18 and 19 as ChPs. The GSD indicates that the mean size on the terrain is 5.18 cm. The distribution of the points is shown in Figure 8, together with the orthomosaic obtained from Scenario C.

Table 5. Mean RMSE of the GCP and ChP for the four Block 1 scenarios (in cm).

| Scenario | Type | Point | East | North | Altitude | RMSE | Mean RMSE |
|----------|------|-------|-------|-------|----------|------|-----------|
| A | GCP | 1 | 4.9 | 2.9 | −0.2 | 5.7 | 5.4 |
| | | 2 | −0.9 | −4.2 | 0.2 | 4.3 | |
| | | 3 | −1.5 | 6.5 | 0.2 | 6 | |
| | | 4 | −2.5 | −5.1 | −0.2 | 5.7 | |
| | ChP | 18 | 7.5 | 15.1 | 5.5 | 17.7 | 11.4 |
| | | 19 | −2.9 | −3.7 | −1.8 | 5.1 | |
| B | GCP | 1 | 5.1 | 2.1 | −0.1 | 5.5 | 5.2 |
| | | 2 | −1.7 | −3.9 | 0.03 | 4.3 | |
| | | 3 | −0.4 | 5.9 | 0.07 | 5.9 | |
| | | 4 | −3 | −4.1 | −0.1 | 5.1 | |
| | ChP | 18 | 9.9 | 12.3 | 0.7 | 15.8 | 11 |
| | | 19 | −5.3 | −2.7 | −1.6 | 6.2 | |
| C | GCP | 1 | 3.5 | 1.8 | −0.1 | 3.9 | 3.6 |
| | | 2 | −1.1 | −2.9 | 0.05 | 3.1 | |
| | | 3 | −0.7 | 3.9 | 0.08 | 3.9 | |
| | | 4 | −1.7 | −2.8 | −0.08 | 3.3 | |
| | ChP | 18 | 7 | 13.7 | 4.2 | 16 | 11.4 |
| | | 19 | −6.2 | −2.5 | 1.1 | 6.8 | |
| D | GCP | 1 | 5.5 | 2.8 | 0.1 | 6.1 | 5.3 |
| | | 2 | −1.9 | −4.4 | −0.1 | 4.7 | |
| | | 3 | −1.3 | 5.6 | −0.1 | 5.7 | |
| | | 4 | −2.3 | −3.9 | 0.1 | 4.5 | |
| | ChP | 18 | 8.1 | 12.6 | 1.2 | 14.9 | 14.2 |
| | | 19 | −13.2 | 0.3 | −2.1 | 13.4 | |

3.2.2. Block 2 Results

Block 2 covers an approximate area of 19 ha. The GCPs continued to be distributed at the four corners of the block; points 3A and 4A were the same as in Block 1 (Figure 4), and points 5A and 6A were the same as in Block 3. Figure 9 shows the results of the RMSE for the GCPs and ChPs in the four scenarios studied. The GSD was 6.22 cm for Scenario A, 5.15 cm for Scenario B, 5.48 cm for Scenario C, and 4.26 cm for Scenario D.

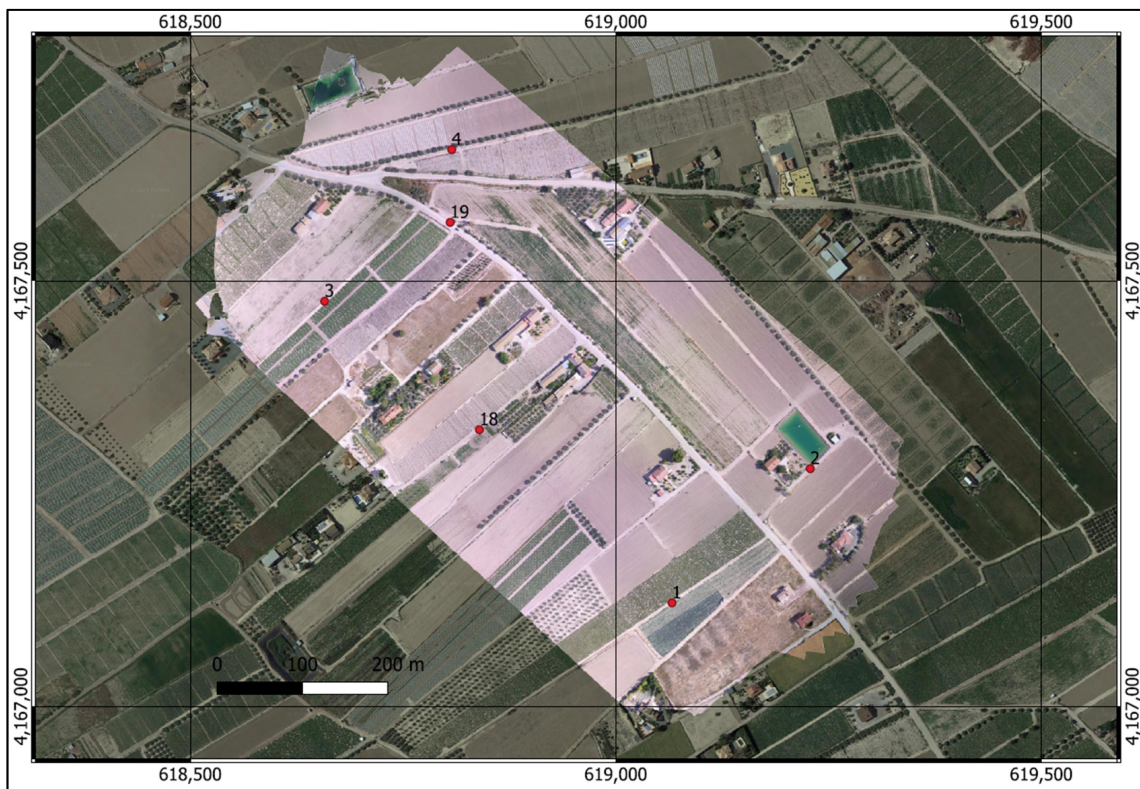


Figure 8. Orthophotograph of Block 1 created after the photogrammetric process; background image from Google Satellite orthophotograph. The GCPs are shown distributed at the four corners of Block 1 for the four scenarios (points 1, 2, 3, and 4); points 18 and 19 were left as ChPs.

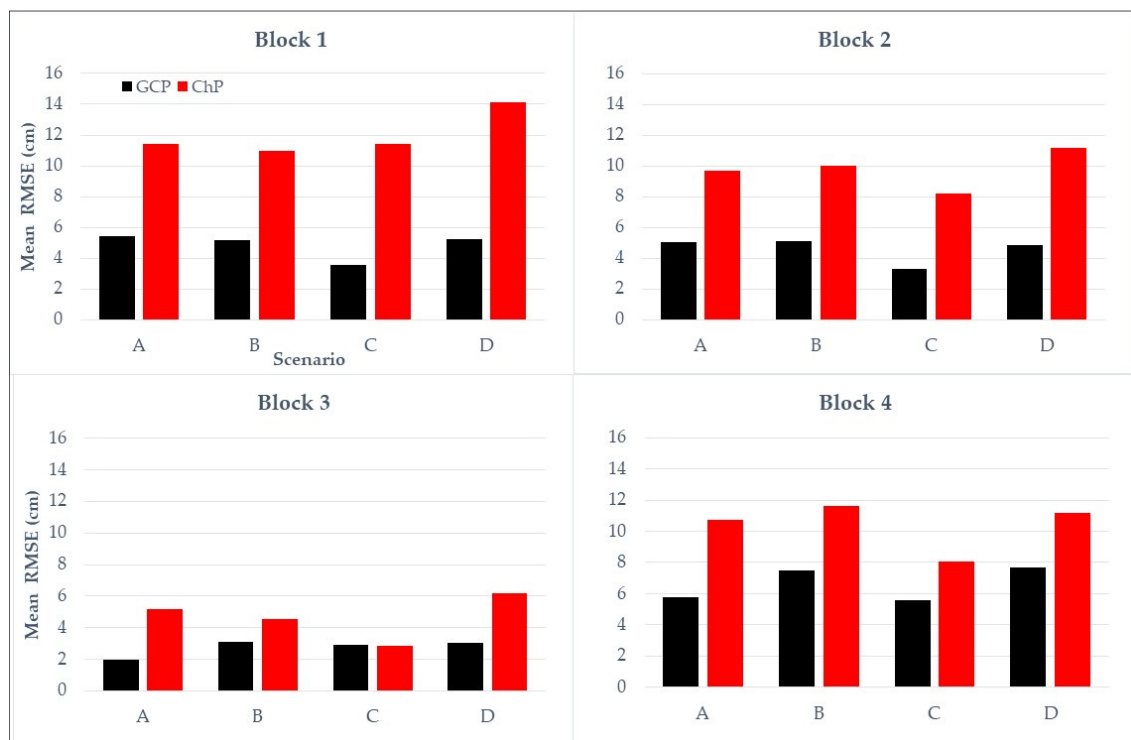


Figure 9. Distribution of the mean RMSE of the GCPs and ChPs of the four blocks for the scenarios studied (for A, B, C & D, vid. Section 2.3 and Figure 7).

3.2.3. Block 3 Results

The block covers an approximate area of 23 ha. The GCPs continued to be distributed at the four corners; points 5 and 6 were the same as in Block 2, and points 7 and 6 were the same as in Block 4. Figure 9 shows the results of the RMSE for the GCPs and ChPs. The GSD was 3.05 cm for Scenario A, 3.03 cm for Scenario B, 3.32 cm for Scenario C, and 3.3 cm for Scenario D.

3.2.4. Block 4 Results

The block measures an approximate area of 18.8 ha. The GCPs continued to be distributed at the four corners; points 7 and 6 were the same as in Block 3. Figure 9 shows the results of the RMSE for the GCPs and ChPs. The GSD was 6.12 cm for Scenario A, 6.11 cm for Scenario B, 5.53 cm for Scenario C, and 4.47 cm for scenario D.

3.3. Accuracy of the Photogrammetric Survey

The mean of the RMSE, GCPs, and ChPs, was calculated for the four blocks studied in the four scenarios (Figure 9).

3.4. Calculation of the A Priori Accuracy Parameters for the Block

To develop Equation (2), described in the methodology (Section 2.4), and estimate the value of the multiplication factor of the μ_{XYZ} photogrammetric block, the values of σ_0 were taken as the projection error of each block resulting from the Agisoft Metashape report (Table 6), and the mean of the RMSE for the GCPs and ChPs separately (Table 5). It is thus possible to calculate the coefficient to determine the weight for each scenario and average them with the four blocks. The results of this factor (for both GCPs and ChPs), with the corresponding standard deviation, can be seen in Table 7.

Table 6. Parameters for the calculation of μ_{XYZ} from the adjustments using Agisoft Metashape for each scenario in the four blocks.

| | SCENARIO | GSD (cm) | PROJ. ERROR (σ_0) |
|---------|----------|----------|----------------------------|
| BLOCK 1 | A | 5.2 | 0.7 |
| | B | 5.2 | 0.7 |
| | C | 4.7 | 0.7 |
| | D | 4.5 | 0.9 |
| BLOCK 2 | A | 6.2 | 0.7 |
| | B | 5.2 | 0.8 |
| | C | 5.5 | 0.8 |
| | D | 4.3 | 1.1 |
| BLOCK 3 | A | 3.1 | 0.6 |
| | B | 3.3 | 0.7 |
| | C | 3 | 0.7 |
| | D | 3.3 | 0.9 |
| BLOCK 4 | A | 6.1 | 0.7 |
| | B | 6.1 | 0.8 |
| | C | 5.5 | 0.7 |
| | D | 4.5 | 0.9 |

Table 7. Mean μ_{xyz} and std μ_{xyz} of the GCPs and ChPs for the four scenarios. The best results are presented in green and the worst in red.

| SCENARIO | μ_{xyz} GCP | μ_{xyz} ChP | std μ_{xyz} GCP | std μ_{xyz} ChP |
|----------|-----------------|-----------------|---------------------|---------------------|
| A | 1.2 | 2.6 | 0.2 | 0.5 |
| B | 1.2 | 2.3 | 0.2 | 0.6 |
| C | 1.0 | 2.1 | 0.3 | 0.8 |
| D | 1.2 | 2.8 | 0.1 | 0.6 |

The accuracy factor in the three μ_{xyz} components depends on the scenario selected for the UAV flight planning, the GSD, and the posterior sigma naught of the bundle block adjustment (σ_0); in case this latter value is unknown by the user, it can be set equal to 1.

4. Discussion

The planning of the UAV-DAP flights is key for obtaining the centimetric level of accuracy. One aspect to consider is the accuracy of the GCPs, being recommended to be less than the GSD. The mean in this study was 7 mm, which was less than the GSD. The GCPs and ChPs must also be located in places visible in the photo acquisition and must not impede the GNSS signal.

The study area was divided into four blocks, and four different scenarios were analysed. Scenarios A and B generated error results above the GSD. Scenario C, which has cross strips at the edges of the block where the GCP are located, produced the highest accuracy in planimetry and altimetry. These results reveal that option C, with a GCP at each corner and a cross strip at each end of the block at a lower height (less than 10 m), delivered an RMSE below the GSD in the four blocks studied, confirming that the cross strips at the edges of the block increase the accuracy, in aerial triangulation flights with GNSS and INS (Inertial Navigation Systems) [31], up to 23%, if compared the ChPs using conventional flight planning software (Scenario A vs. Scenario C, Table 7). Scenario D, which contemplates the sum of all the previous scenarios, did not show any significant improvement, all the way around, due to the excessively high overlap among the three crossing strips. As it has a greater number of photographs with surplus cover in the cross strips, it requires longer for both the data acquisition and processing phases.

It can be confirmed that the RMSE of the ChP is more than two times higher than the GSD and is smallest in Scenario C, where it has a better performance in three of the four cases.

The four scenarios have acceptable accuracies in aerial photogrammetry, as they are within the range of 1–2 GSD in planimetry and 2–3 GSD in altimetry [28]. This is thanks to the quality of the data collection on the ground, as well as the planning and processing strategies. A comparison of the results in Table 1 by the authors of [26], with a ratio of 0.29 GCP/ha, similar to this study with 0.2 GCP/ha, shows a decrease in the value of the RMSE, which falls from 5.9 cm to 2.9 cm for Scenario C; this result can be explained by the improvement obtained when the cross strips are made perpendicular to the block. The study in [44] also shows that for the best results in planimetry, the GCP must be located at the corners of the study area, and to improve the accuracy in the vertical component, it is necessary to use a well-distributed GCPs density between 0.5–1 GCP/ha; however, the GCPs must be located at the edges of the block, as the points measured in the centre do not produce any significant improvement in the adjustment, as evidenced in the study. The research of [43,44] conclude that to improve the vertical and horizontal accuracy, it is advisable to use the GCPs at the ends of the block, as can also be deduced from this research. However, other studies with UAVs [14,16] demonstrate that a higher number of images affects the accuracy of the photogrammetric survey.

The objectives, such as the type of information required, must be established before planning the flight to obtain results that comply with the tolerance of the work and avoid unnecessarily exceeding the number of photographs taken with the UAVs, the flight height, or the number of GCPs. Another aspect worth considering is that in the literature on photogrammetry, there is a clear consensus as to the quantity and location of the GCP, where the accuracy can only be compensated with chains of GCPs perpendicular to the flight strips, or by employing cross strips at the ends, while leaving the GCPs at the corners or on the perimeter of the block. This produces better results for RMSE in regards to east, north, and altitude, as shown in Scenario C.

In this investigation, the same calculations were recomputed, adding a 5th GCP in the centre of each block, to check whether or not the incorporation of an additional GCP might have yielded a significant improvement. The Supplementary Material presents the results achieved in Tables S1–S4, and their mean values are summarised in Figure S1. The addition

of one additional central GCP in the middle does not yield a significant improvement in the photogrammetric mode, as it can be checked with the RMSE on the GCPs, and it slightly enlarges the RMSE on the ChPs. Thus, including a single GCP in the centre of each block corroborates the error budget for planimetry accuracy [49]. The authors of [50] suggest the addition of convergent images to avoid the doming effect in the topographic models derived from UAV; alternatively, they also suggest adding control measurements. In this sense, we can confirm that the addition of transversal strips is also highly recommended, as suggested by the study in [47]; we confirmed this option for lower flying heights. In fact, the positive effect of including convergent images can also be obtained including lower flying cross strips, to appropriately determine the geometric camera calibration of the UAV-DAP survey (Scenario C).

In regard to the a priori accuracy calculations obtained in Table 6, it can be seen that Scenario C has the lowest results for the multiplying factor in the GCPs and ChPs, and these are therefore the reference values selected as the best procedure for this type of flight. Better results are obtained when verifying the accuracy of the simple model compared with that used in [49], so with these new parameters, the accuracy can be estimated using Equation (3), described in the methodology, before conducting the flight, provided that cross strips, or otherwise, dense GCP perpendicular chains, are used at the edges of the block. To verify the accuracy, it is recommended to use the value of μ_{xyz} ChPs, as these points show the accuracy of the photogrammetric adjustment not in the GCPs but in the ChPs.

This study also demonstrates the influence of the type of camera used, as specified in Table 3. The Zenmuse X5S camera achieves accuracies below 3 cm in the case of Block 3, and the DJI FC300X camera has an accuracy of 6 cm in the case of Blocks 1, 2, and 4 in Scenarios A, B, and D.

Another important aspect to consider when measuring vast areas is that the flights can be divided into blocks, sharing the same GCPs at the edges and the lower cross strips, thereby reducing the topographic control required and ensuring a lower consumption of batteries, a limiting factor in multirotor UAVs.

5. Conclusions

This article has analysed the accuracy that can be obtained on flat terrains from UAV-DAP. In addition to the classic aerial flight planning setup with near-parallel imaging directions in forwarding strips, three additional scenarios are analysed using only four GCPs, one at each end, plus one additional GCP in the centre (see Supplementary Material). The research conducted on four blocks confirms that the error achieved in the adjustment of the photogrammetric block is heavily dependent on flight planning. In this case, it is confirmed that the best results are obtained by adding lower flying heights cross strips at both ends, an aspect that is not included in the current flight planning programs (for example, DroneDeploy, PIX4D).

Reinforcing the conventional flights with lower cross strips achieves greater accuracy in the UAV-DAP. A single cross strip at each end, with the GCPs located at the corners of the block, is sufficient to improve the accuracy. When three flight strips are used, together with perimeter strips, as in Scenario D, the error increases significantly by 28.9%, considering the ChPs. Therefore, scenarios with extremely short baselengths, with multiple cross strips, are highly discouraged, even with lower flying heights.

If Scenario C is applied, instead of the one proposed by the DroneDeploy software [39] (Scenario B), the precision increases by 9.2%, thus guaranteeing better results for the products obtained, namely the DTMs and orthomosaics, with four GCPs and with lower battery consumption on flat terrains. The classic implementation of flight planning, Solution A, is the least advisable, as the RMSE in the ChPs is up to 23% larger than in Scenario C.

Future analyses will study the effect of including oblique flight strips (equivalent to convergent imagery in terrestrial photogrammetry), scenarios with mountainous terrains or larger areas, and different numbers of GCPs under other flying options (e.g., double grid acquisition for urban areas).

Supplementary Materials: The following supporting information can be downloaded at: <https://www.mdpi.com/article/10.3390/rs14122877/s1>, Figure S1: Distribution of the mean RMSE of the GCPs and ChPs of the four blocks for the scenarios studied, with four GCPs at the corners and one in the middle; Table S1: Mean RMSE of the GCP and ChP for the four Block 1 scenarios; Table S2: Mean RMSE of the GCP and ChP for the four Block 2 scenarios; Table S3: Mean RMSE of the GCP and ChP for the four Block 3 scenarios; Table S4: Mean RMSE of the GCP and ChP for the four Block 4 scenarios.

Author Contributions: Conceptualisation, J.L.L.; Data acquisition, J.P.C.-R., A.N.A.-V., J.F.P. and J.L.L.; Formal analysis, J.F.; Funding acquisition, J.L.L. and J.F.; Investigation, A.N.A.-V., J.P.C.-R. and J.L.L.; Methodology, J.L.L.; Software, A.N.A.-V., J.F.P. and J.P.C.-R.; Supervision, J.L.L. and J.F.; Validation, J.F.P.; Writing—original draft, A.N.A.-V.; Writing—review & editing, J.L.L., J.F.P., J.P.C.-R. and J.F. All authors have read and agreed to the published version of the manuscript.

Funding: The work has been partly supported by Spanish Agencia Estatal de Investigación (10.13039/501100011033) grant RTI2018-093874-B-I00 (DEEP-MAPS). This work represents a contribution to CSIC Thematic Interdisciplinary Platform PTI TELEDETECT.

Data Availability Statement: Not applicable.

Conflicts of Interest: The authors declare no conflict of interest.

References

- Mancini, F.; Dubbini, M.; Gattelli, M.; Stecchi, F.; Fabbri, S.; Gabbianelli, G. Using Unmanned Aerial Vehicles (UAV) for High-Resolution Reconstruction of Topography: The Structure from Motion Approach on Coastal Environments. *Remote Sens.* **2013**, *5*, 6880–6898. [[CrossRef](#)]
- Varbla, S.; Ellmann, A.; Puust, R. Centimetre-Range Deformations of Built Environment Revealed by Drone-Based Photogrammetry. *Autom. Constr.* **2021**, *128*, 103787. [[CrossRef](#)]
- Colomina, I.; Molina, P. Unmanned Aerial Systems for Photogrammetry and Remote Sensing: A Review. *ISPRS J. Photogramm. Remote Sens.* **2014**, *92*, 79–97. [[CrossRef](#)]
- Moe, K.T.; Owari, T.; Furuya, N.; Hiroshima, T. Comparing Individual Tree Height Information Derived from Field Surveys, LiDAR and UAV-DAP for High-Value Timber Species in Northern Japan. *Forests* **2020**, *11*, 223. [[CrossRef](#)]
- Sanz-Ablanedo, E.; Chandler, J.H.; Rodríguez-Pérez, J.R.; Ordóñez, C. Accuracy of Unmanned Aerial Vehicle (UAV) and SfM Photogrammetry Survey as a Function of the Number and Location of Ground Control Points Used. *Remote Sens.* **2018**, *10*, 1606. [[CrossRef](#)]
- Doorn, A.J.; Van Koenderink, J.J. Affine Structure from Motion. *JOSA A* **1991**, *8*, 377–385. [[CrossRef](#)]
- Giordan, D.; Hayakawa, Y.; Nex, F.; Remondino, F.; Tarolli, P. Review Article: The Use of Remotely Piloted Aircraft Systems (RPASs) for Natural Hazards Monitoring and Management. *Nat. Hazards Earth Syst. Sci.* **2018**, *18*, 1079–1096. [[CrossRef](#)]
- Nettis, A.; Saponaro, M.; Nanna, M. RPAS-Based Framework for Simplified Seismic Risk Assessment of Italian RC-Bridges. *Buildings* **2020**, *10*, 150. [[CrossRef](#)]
- Contreras-De-villar, F.; García, F.J.; Muñoz-Perez, J.J.; Contreras-De-villar, A.; Ruiz-Ortiz, V.; Lopez, P.; Garcia-López, S.; Jigena, B. Beach Leveling Using a Remotely Piloted Aircraft System (Rpas): Problems and Solutions. *J. Mar. Sci. Eng.* **2021**, *9*, 19. [[CrossRef](#)]
- Monteiro, J.G.; Jiménez, J.L.; Gizzi, F.; Přikryl, P.; Lefcheck, J.S.; Santos, R.S.; Canning-Clode, J. Novel Approach to Enhance Coastal Habitat and Biotope Mapping with Drone Aerial Imagery Analysis. *Sci. Rep.* **2021**, *11*, 574. [[CrossRef](#)]
- Siebert, S.; Teizer, J. Mobile 3D Mapping for Surveying Earthwork Projects Using an Unmanned Aerial Vehicle (UAV) System. *Autom. Constr.* **2014**, *41*, 1–14. [[CrossRef](#)]
- Galeana Pérez, V.M.; Chávez Alegría, O.; Medellín Aguilar, G. On the Measure of Land Subsidence throughout DEM and Orthomosaics Using GPS and UAV. *Ing. Investig. Tecnol.* **2021**, *22*, 1–12. [[CrossRef](#)]
- Miró Moncho, A. *Optimización de La Geometría Alar de Un UAS/RPAS Para La Vigilancia Antiincendios*; Polytechnic University of Valencia: Valencia, Spain, 2018.
- Ahmad, A.; Ordoñez, J.; Cartujo, P.; Martos, V. Remotely Piloted Aircraft (RPA) in Agriculture: A Pursuit of Sustainability. *Agronomy* **2020**, *11*, 7. [[CrossRef](#)]
- Araujo, R.F.; Chambers, J.Q.; Celes, C.H.S.; Muller-Landau, H.C.; dos Santos, A.P.F.; Emmert, F.; Ribeiro, G.H.P.M.; Gimenez, B.O.; Lima, A.J.N.; Campos, M.A.A.; et al. Integrating High Resolution Drone Imagery and Forest Inventory to Distinguish Canopy and Understory Trees and Quantify Their Contributions to Forest Structure and Dynamics. *PLoS ONE* **2020**, *15*, e0243079. [[CrossRef](#)] [[PubMed](#)]
- Baron, J.; Hill, D.J. Monitoring Grassland Invasion by Spotted Knapweed (*Centaurea maculosa*) with RPAS-Acquired Multispectral Imagery. *Remote Sens. Environ.* **2020**, *249*, 112008. [[CrossRef](#)]
- Gabara, G.; Sawicki, P. Multi-Variant Accuracy Evaluation of UAV Imaging Surveys: A Case Study on Investment Area. *Sensors* **2019**, *19*, 5229. [[CrossRef](#)]

18. Polat, N.; Uysal, M. An Experimental Analysis of Digital Elevation Models Generated with Lidar Data and UAV Photogrammetry. *J. Indian Soc. Remote Sens.* **2018**, *46*, 1135–1142. [[CrossRef](#)]
19. Acevo Herrera, R. Sistemas de Teledetección Activos y Pasivos Embarcados en Sistemas Aéreos No Tripulados para la Monitorización de la Tierra. Ph.D. Thesis, Universitat Politècnica Catalunya, Barcelona, Spain, 2011.
20. Boletín Oficial del Estado (BOE). Real Decreto 1036/2017 de 15 de Diciembre. *Bol. Estado* **2017**, *316*, 129609–129641.
21. Gómez-López, J.M.; Pérez-García, J.L.; Mozas-Calvache, A.T.; Delgado-García, J. Mission Flight Planning of RPAS for Photogrammetric Studies in Complex Scenes. *ISPRS Int. J. Geo-Inf.* **2020**, *9*, 392. [[CrossRef](#)]
22. Lerma, J.L.G. *Fotogrametría Moderna: Analítica y Digital*; Universitat Politècnica de València: Valencia, Spain, 2002; 560p, ISBN 978-84-9705-210-8.
23. Akturk, E.; Altunel, A.O. Accuracy Assessment of a Low-Cost UAV Derived Digital Elevation Model (DEM) in a Highly Broken and Vegetated Terrain. *Meas. J. Int. Meas. Confed.* **2019**, *136*, 382–386. [[CrossRef](#)]
24. Agüera-Vega, F.; Carvajal-Ramírez, F.; Martínez-Carricondo, P. Assessment of Photogrammetric Mapping Accuracy Based on Variation Ground Control Points Number Using Unmanned Aerial Vehicle. *Meas. J. Int. Meas. Confed.* **2017**, *98*, 221–227. [[CrossRef](#)]
25. Uysal, M.; Toprak, A.S.; Polat, N. DEM Generation with UAV Photogrammetry and Accuracy Analysis in Sahitler Hill. *Meas. J. Int. Meas. Confed.* **2015**, *73*, 539–543. [[CrossRef](#)]
26. Jiménez-Jiménez, S.I.; Ojeda-Bustamante, W.; Ontiveros-Capurata, R.E.; Flores-Velázquez, J.; Marcial-Pablo, M.d.J.; Robles-Rubio, B.D. Quantification of the Error of Digital Terrain Models Derived from Images Acquired with UAV. Cuantificación del Error de Modelos Digitales de Terreno Derivados de Imágenes Adquiridas Con UAV. *Ing. Agríc. Biosist.* **2017**, *9*, 85–100. [[CrossRef](#)]
27. Cisneros, S.; García, É.; Montoya, K.; Sinde, I. Study of the Configurations of Ground Control Points for Photogrammetry with Drone. *Rev. Geospac.* **2019**, *16*, 43–57. [[CrossRef](#)]
28. Casella, V.; Chiabrande, F.; Franzini, M.; Manzano, A.M. Accuracy Assessment of a UAV Block by Different Software Packages, Processing Schemes and Validation Strategies. *ISPRS Int. J. Geo-Inf.* **2020**, *9*, 164. [[CrossRef](#)]
29. Gómez-Candón, D.; De Castro, A.I.; López-Granados, F. Assessing the Accuracy of Mosaics from Unmanned Aerial Vehicle (UAV) Imagery for Precision Agriculture Purposes in Wheat. *Precis. Agric.* **2014**, *15*, 44–56. [[CrossRef](#)]
30. Reshetyuk, Y.; Mårtensson, S.G. Generation of Highly Accurate Digital Elevation Models with Unmanned Aerial Vehicles. *Photogramm. Rec.* **2016**, *31*, 143–165. [[CrossRef](#)]
31. Zimmerman, T.; Jansen, K.; Miller, J. Analysis of UAS Flight Altitude and Ground Control Point Parameters on DEM Accuracy along a Complex, Developed Coastline. *Remote Sens.* **2020**, *12*, 2305. [[CrossRef](#)]
32. Martínez-Carricondo, P.; Agüera-Vega, F.; Carvajal-Ramírez, F.; Mesas-Carrascosa, F.J.; García-Ferrer, A.; Pérez-Porras, F.J. Assessment of UAV-Photogrammetric Mapping Accuracy Based on Variation of Ground Control Points. *Int. J. Appl. Earth Obs. Geoinf.* **2018**, *72*, 1–10. [[CrossRef](#)]
33. Arévalo-Verjel, A.N.; Lerma, J.L.; Fernández, J. Análisis Comparativo de Software Para Obtener MDT Con Fotogrametría RPAS. In Proceedings of the Tercer Congreso en Ingeniería Geomática, Valencia, Spain, 7–8 July 2021; pp. 209–215.
34. Tomaščík, J.; Mokroš, M.; Surový, P.; Grznárová, A.; Merganič, J. UAV RTK/PPK Method—An Optimal Solution for Mapping Inaccessible Forested Areas? *Remote Sens.* **2019**, *11*, 721. [[CrossRef](#)]
35. Fernandez, J.; Prieto, J.F.; Escayo, J.; Camacho, A.G.; Luzón, F.; Tiampo, K.F.; Palano, M.; Abajo, T.; Pérez, E.; Velasco, J.; et al. Modeling the Two- and Three-Dimensional Displacement Field in Lorca, Spain, Subsidence and the Global Implications. *Sci. Rep.* **2018**, *8*, 14782. [[CrossRef](#)] [[PubMed](#)]
36. González, P.J.; Fernández, J. Drought-Driven Transient Aquifer Compaction Imaged Using Multitemporal Satellite Radar Interferometry. *Geology* **2011**, *39*, 551–554. [[CrossRef](#)]
37. Bonì, R.; Herrera, G.; Meisina, C.; Notti, D.; Béjar-Pizarro, M.; Zucca, F.; González, P.J.; Palano, M.; Tomás, R.; Fernández, J.; et al. Twenty-Year Advanced DInSAR Analysis of Severe Land Subsidence: The Alto Guadalentín Basin (Spain) Case Study. *Eng. Geol.* **2015**, *198*, 40–52. [[CrossRef](#)]
38. Ezquerro, P.; Tomás, R.; Béjar-Pizarro, M.; Fernández-Merodo, J.A.; Guardiola-Albert, C.; Staller, A.; Sánchez-Sobrino, J.A.; Herrera, G. Improving Multi-Technique Monitoring Using Sentinel-1 and Cosmo-SkyMed Data and Upgrading Groundwater Model Capabilities. *Sci. Total Environ.* **2020**, *703*, 134757. [[CrossRef](#)]
39. Drone Mapping Software. Available online: <https://www.dronedeploy.com/> (accessed on 3 June 2021).
40. Dach, R.; Schaer, S.; Arnold, D.; Kalarus, M.S.; Prange, L.; Stebler, P.; Villiger, A.; Jäggi, A. *CODE Final Product Series for the IGS*; Astronomical Institute, University of Bern: Bern, Switzerland, 2016.
41. Teunissen, P.J.G.; Montenbruck, O. *Springer Handbook of Global Navigation Satellite Systems*; Springer International Publishing: Cham, Switzerland, 2017.
42. Boehm, J.; Werl, B.; Schuh, H. Troposphere Mapping Functions for GPS and Very Long Baseline Interferometry from European Centre for Medium-Range Weather Forecasts Operational Analysis Data. *J. Geophys. Res. Solid Earth* **2006**, *111*, 2406. [[CrossRef](#)]
43. Velasco, J.; Herrero, T.; Molina, I.; López, J.; Pérez-Martín, E.; Prieto, J. Methodology for Designing, Observing and Computing of Underground Geodetic Networks of Large Tunnels for High-Speed Railways. *Inf. Constr.* **2015**, *67*, e076. [[CrossRef](#)]
44. Velasco-Gómez, J.; Prieto, J.F.; Molina, I.; Herrero, T.; Fábrega, J.; Pérez-Martín, E. Use of the Gyrotheodolite in Underground Networks of Long High-Speed Railway Tunnels. *Surv. Rev.* **2016**, *48*, 329–337. [[CrossRef](#)]

45. ArcGIS for Desktop. Available online: <https://desktop.arcgis.com/es/arcmap/10.3/manage-data/kml/what-is-kml-.htm> (accessed on 3 June 2021).
46. Agisoft PhotoScan User Manual—Professional Edition, Version 1.2. 2016. Available online: https://www.agisoft.com/pdf/photoscan-pro_1_2_en.pdf (accessed on 2 June 2021).
47. Kraus, K. Volume 2, Advanced Methods and Applications. In *Photogrammetry*; Jansa, J., Kager, H., Eds.; Dümmler: Bonn, Germany, 1997; p. 459. ISBN 3427786943.
48. FGDC-STD-007.3-1998; Geospatial Positioning Accuracy Standards, Part 3: National Standard for Spatial Data Accuracy. Subcommittee for Base Cartographic Data, Federal Geographic Data Committee: Reston, VA, USA, 1998.
49. Kraus, K. Volume 1, Fundamentals and Standard Processes. In *Photogrammetry*; Dümmler: Bonn, Germany, 1993; p. 389, ISBN 3427786846.
50. James, M.R.; Robson, S. Mitigating Systematic Error in Topographic Models Derived from UAV and Ground-Based Image Networks. *Earth Surf. Process. Landf.* **2014**, *39*, 1413–1420. [[CrossRef](#)]